UDK 544.532.122
Original scientific article/Izvirni znanstveni članek

ISSN 1580-2949
MTAEC9, 56(4)397(2022)

LASER DRILLING OF AIR-FILM COOLING HOLES IN AIR AND WITH COAXIAL WATERJET ASSISTANCE

LASERSKO VRTANJE ZRAČNO HLAJENIH IZVRTIN Z DODATNO POMOČJO KOAKSIALNEGA CURKA VODE

Dongjie Wu[1], Bin Wang[2], Yuezhuan Liu[1,2*]

[1]School of Mechanical Engineering, Ningbo University of Technology, Ningbo, China
[2]Ningbo Institute of Material Technology and Engineering, Chinese Academy of Science, Ningbo, China

Prejem rokopisa – received: 2022-05-17; sprejem za objavo – accepted for publication: 2022-06-20

doi:10.17222/mit.2022.497

Air-film cooling holes were drilled into a turbine blade with a 532-nm Nd:YVO_4 nanosecond laser in air and with coaxial waterjet assistance. The drilling quality of the sidewalls of the holes was investigated comparatively by means of a 3D confocal laser scanning microscope, scanning electron microscopy, transmission electron microscopy, X-ray diffraction and energy-dispersive X-ray spectroscopy. Results have shown that the maximum thickness of the processing-induced defects around the air-film cooling holes drilled by the laser in air is up to 100 μm, while the holes obtained by means of the asynchronous operation of laser drilling in air and coaxial waterjet assistance indicate no spatter, oxide layer, recast layer or cracks. Compared with laser drilling in air, the minimum size of the heat-affected zone around the air-film cooling holes induced by asynchronous processing is decreased down to the sub-micrometer scale. The main phases in the oxide layer, recast layer and heat-affected zone are α-Al_2O_3, γ-Ni and β-NiAl, respectively. Asynchronous processing can help us achieve high position precision and it will have wide application.

Keywords: coaxial waterjet assisted laser drilling, air-film cooling holes, heat-affected zone, scanning electron microscopy, transmission electron microscopy

Avtorji v članku opisujejo vrtanje izvrtin na turbinskih lopaticah, hlajenih z zračnim filmom. Vrtanje je bilo izvedeno s 532 nano-meterskim neodim-itrij vanadij oksidnim (Nd:YVO_4) nano-sekundnim laserjem na zraku in z dodatno pomočjo koaksialnega vodnega curka. Kakovost vrtanja stranskih sten izvrtin so primerjalno raziskovali s tri dimenzionalnim (3D) konfokalnim laserskim vrstičnim mikroskopom, klasičnim vrstičnim in presevnim elektronskim mikroskopom (SEM in TEM), rentgensko difrakcijo (XRD) ter energijsko disperzijsko spektroskopijo rentgenskih žarkov (EDXS). Rezultati raziskave so pokazali, da je maksimalna debelina procesno induciranih poškodb okoli zračno hlajenih lasersko vrtanih izvrtin do 100 μm, medtem ko pri tistih izvrtinah, ki so bile izdelane z asinhronim procesom koaksialnega vodnega curka ni bilo opaziti obrizgov, oksidnega filma, pretaljene plasti in razpok. V primerjavi z zračno hlajenim laserskim vrtanjem se je pri asistenčnem asinhronem procesu vrtanja zmanjšala debelina toplotno vplivane cone na sub-mikronsko raven. Glavne faze, prisotne v oksidni in pretaljeni plasti ter toplotno vplivani coni so bile: α-Al_2O_3, γ-Ni in β-NiAl. Avtorji v zaključku ugotavljajo, da lahko z opisanim asinhronim procesom dosežemo večjo pozicijsko natančnost vrtanja, kar bi lahko bilo uporabno tudi na mnogih drugih področjih.

Ključne besede: lasersko vrtanje s pomočjo koaksialnega vodnega curka, zračno hlajene izvrtine, toplotno vplivana cona, vrstična mikroskopija, presevna elektronska mikroskopija

1 INTRODUCTION

With the advantages including toughness, creep strength and hot-corrosion resistance at high temperatures, nickel-based single-crystal superalloys have been utilized to manufacture hot-zone components of aircraft and power generation turbine engines for decades.[1] Modern aircraft engines contain up to 100 000 air-film cooling holes (AFCHs) with the diameters of 0.5–1 mm in the hot-zone components, which can reduce the surface temperature of these components.[2] Due to the protection of AFCHs and thermal barrier coatings (TBCs), the working temperature of the blade substrate is reduced from app. 1500 °C to app. 1150 °C in advanced turbine engines.[3] For the TBC-coated hot-zone components, AFCHs are often made by laser drilling.[4]

The AFCHs drilled with conventional lasers, such as millisecond, microsecond and continuous wave lasers, usually induce extensive metallurgical defects around the sidewalls.[5] Delamination of TBCs often takes place after the laser drilling in air (LDIA) and the main metallurgical defects include oxide layer, recast layer and heat-affected zone (HAZ).[6] The HAZ is defined as a region of the target materials surrounding the laser beam focused zone that has not melted but has experienced microstructural evolutions due to the heat conduction during laser drilling. Metallurgical defects will unavoidably affect the mechanical and cooling properties of the hot-zone components with AFCHs.[7] In order to reduce the metallurgical defects induced by the conventional lasers, ultrafast lasers including picosecond and femtosecond lasers have been utilized to drill AFCHs in recent years. However, picosecond and femtosecond laser drillings take a longer time for machining AFCHs than

*Corresponding author's e-mail:
yzliu10b@alum.imr.ac.cn (Yuezhuan Liu)

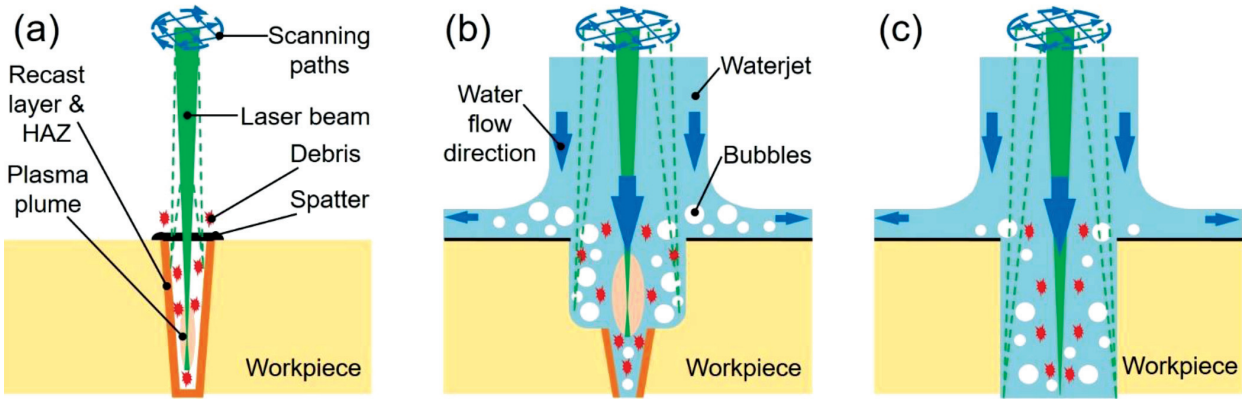

Figure 1: Schematic diagram of LDIA + CWALD: a) LDIA, b) hole expansion with CWALD, c) end of process

nanosecond laser drilling.[8] Through a series of observations of the micro-machining quality of metallic and non-metallic materials, it has been found that nanosecond laser drilling not only decreases the metallurgical defects compared to the conventional laser drilling, but also costs less, drills deeper and faster than the picosecond and femtosecond laser drilling.[9] Nevertheless, there is very little published information concerning the nanosecond laser drilling of AFCHs. Therefore, it is necessary to study the process of nanosecond laser drilling and reduce metallurgical defects during the drilling of AFCHs.

To reduce the metallurgical defects induced by laser machining in air, several new technologies of laser machining have been proposed, such as laser cutting underwater, waterjet-guided laser cutting, microjet water-assisted laser machining, liquid core waveguide laser drilling, coaxial waterjet assisted laser grooving, and coaxial waterjet assisted laser drilling.[10–15] Compared with laser machining in air, the metallurgical defects induced by laser machining underwater or water-assisted laser machining are decreased significantly. However, there is limited literature reporting the combination of LDIA and coaxial waterjet assisted laser drilling (CWALD) of AFCHs in a turbine blade.

In this study, asynchronous operation of AFCHs with LDIA and CWALD (LDIA + CWALD) is proposed for improving the surface quality and drilling efficiency. **Figure 1** shows a schematic diagram of LDIA + CWALD. As shown in **Figure 1a**, the perforation of the workpiece was performed in advance with LDIA, and the diameter of the through-hole was smaller than the target size. This through-hole had a recast layer and HAZ on its inner wall, and there was a taper that could even be large. Then CWALD was used for the hole expansion, making the aperture reach the target size, as shown in **Figure 1b**. Using LDIA + CWALD, as shown in **Figure 1c**, the HAZ and recast layer induced by LDIA could be removed, and a through-hole with a small taper could be obtained.

To test the drilling quality of LDIA + CWALD, the aim of this study was to investigate the microstructural evolution around the AFCHs in turbine blades. The chemical property change and microstructural evolution in the HAZ were characterized using X-ray diffraction (XRD), a 3D confocal laser scanning microscope, a scanning electron microscope (SEM) and a transmission electron microscope (TEM). Results of this work are expected to give a deep insight into the CWALD technology and its promising application in machining AFCHs into turbine blades. This study will broaden the application of CWALD to other fine holes that require high dimensional precision and high processing efficiency with a minimal HAZ.

2 EXPERIMENTAL PART

The material used in this work is a nickel-based single-crystal superalloy. The chemical contents of the materials are listed in **Table 1**.

Table 1: Chemical contents of the nickel-based single-crystal superalloy (*w*/%)

Co	Cr	W	Ta	Al	Mo	Ti	Minor elements	Ni
8.0	8.0	8.0	6.0	5.0	2.0	1.0	0.2Hf, 0.02C, 0.01B	Bal.

Figure 2 shows a schematic diagram and photograph of the experimental set-up for LDIA + CWALD. As shown in **Figure 2a**, the CWALD set-up consists of four main components, a nanosecond solid-state laser and optical system, a water supply system including a diaphragm pump and valves, a laser-water coupling machining head, and a precision five-axis-motion control system. An additional air supply is used to avoid the deposition of spatter inside the nozzle during LDIA. Pure (deionized) water enters the water chamber from the water pipe and is then ejected from the nozzle. **Figure 2b** shows that the galvanometer-controlled laser beam is coupled with the coaxial waterjet through a quartz-glass optical window, after which the laser beam can be used for high-speed scanning motion to produce the required hole types, including micro-grooves, straight holes and

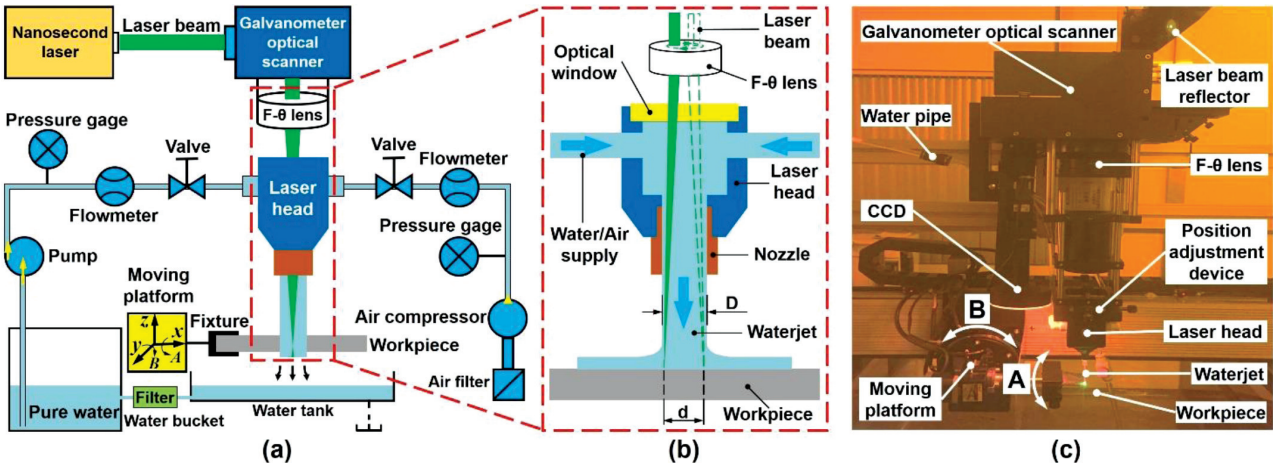

Figure 2: Schematic and photograph of the experimental set-up for LDIA + CWALD: a) diagram of equipment including LDIA and CWALD systems, b) partially enlarged detail from (a) shows a schematic of CWALD, c) five-axis set-up for LDIA + CWALD

Table 2: Main experimental parameters of the LDIA and CWALD

F/(J/cm^2)	P/W	τ/ns	f/kHz	δ/°	D_h/μm	Depth (mm)	v_w/(m/s)
50.00	33.63, 40.37	10, 20	50, 60	90	800	2	1.0 ± 0.05
55.75	37.50, 45.00	10, 20	50, 60	60	700	3	1.5 ± 0.05
65.03	17.50, 43.75	10, 20	20, 50	60	600	4	2.5 ± 0.05
83.63	12.50, 45.00	10, 20	20, 40	30	500	6	2.5 ± 0.05
100.00	26.91	20	20	20	500	6	2.0 ± 0.05

complex-shaped holes. The diameter of the waterjet is larger than that of the target hole, which can reduce the difficulty of the laser and water coupling and improve the coupling stability. With regard to the diameter of the target hole, the diameter of the nozzle in CWALD is generally set at a range of 5–10 mm. In order to reduce the attenuation of laser energy, the pure water should be free of bubbles and move smoothly. Besides acting as the conduction medium of laser, the coaxial waterjet plays the role of cooling the workpiece and removing away ablated materials. **Figure 2c** shows a photograph of the five-axis set-up for LDIA + CWALD.

The light wavelength in a range of 300–600 nm has the lowest energy attenuation in water.[16,17] Therefore, a nanosecond laser with a wavelength of 532 nm is used. The drilling direction of AFCHs is tilted by 20°–90° (the tilt angle, δ) with the tangential direction of the blade surface. The diameter of AFCHs (D_h) is 500–800 μm. In asynchronous processing, the machining diameter of LDIA is 400 μm, and the remaining hole expansion is completed by CWALD. The depth of AFCHs ranges from 2–6 mm. The flow rate of the waterjet (v_w) is up to 2.5 m/s. The F-θ lens holds the focal length of 200 mm. The laser pulse duration (τ) ranges from 10–50 ns. The maximum average power (P) of the laser is up to 50 W. The focal spot diameter (D_f) of the laser beam in air is 42 μm. The D_f of CWALD is 41.4 μm. The laser fluence (F) ranges from 50–100 J/cm^2. The line space of laser scanning is 20 μm. The scanning speed of the laser beam is set at 500 mm/s. The main experimental parameters are given in **Table 2**.

The sections of the drilled turbine blades were cut with a low-speed diamond saw and then they were used for cross-sectional metallographic samples. Some typical samples were lightly etched with a solution of 9.0 % $CuSO_4{\cdot}5H_2O$, 44.5 % H_2SO_4, 2.0 % HCl, and 44.5 % H_2O. The cross-sectional samples were observed with the 3D confocal laser scanning microscope (CLSM, Keyence VX-200) and scanning electron microscope (SEM, FEI Quanta 250). The SEM was equipped with an electron energy dispersive spectrometer, which can detect energy dispersive spectra (EDS) of the target material. Processing-induced defects were investigated using the transmission electron microscope (TEM, FEI G^2 F20) at an accelerating voltage of 200 kV.

3 RESULTS

3.1 Optical observations

Figure 3 shows the entrances of complex-shaped AFCHs drilled by LDIA or/and CWALD. The entrances of the holes drilled by LDIA are completely covered with scorch, while the holes drilled by LDIA + CWALD have no scorch at the entrances and the surface finish is consistent with the blade surface.

Figure 4 presents the microstructures of the cross-sections of the AFCHs drilled at F = 65.03 J/cm^2 and v_w = 2.5 m/s. **Figure 4a** shows the cross-sectional microstructure of the middle section of an AFCH perpendicular to the direction of LDIA. In the process of drilling, the recast layer and HAZ appear around the

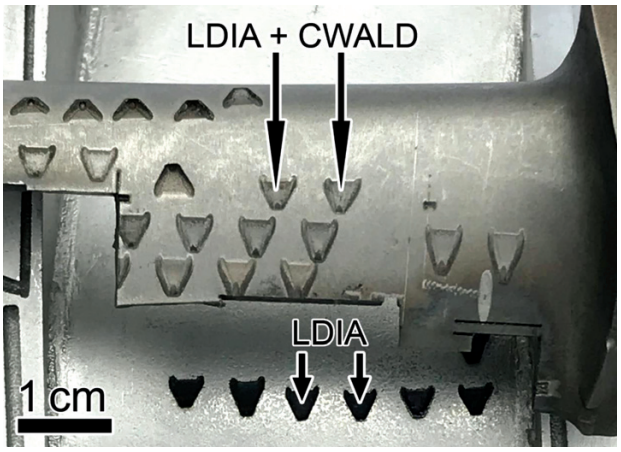

Figure 3: Turbine blade with AFCHs drilled by LDIA and LDIA + CWALD

hole, and their thicknesses are up to 50 μm and 45 μm, respectively. **Figure 4b** shows the cross-sectional microstructure of the middle section of an AFCH perpendicular to the direction of LDIA + CWALD, under the same parameters as in **Figure 4a** and with a laminar waterjet flow rate of 2.5 m/s. A typical $\gamma + \gamma'$ microstructure of the sample up to the edge of the hole indicates that there are no recast layer or HAZ.

Figure 5a displays the cross-sectional microstructure of the mid-section of an AFCH paralleled to the direction of LDIA. The maximum thicknesses of the recast layer and HAZ around the hole are up to 100 μm. The taper induced by the recast layer and HAZ is approximately 3°. **Figure 5b** displays the cross-sectional microstructure of the mid-section of an AFCH paralleled to the direction of LDIA + CWALD under the same parameters as in **Figure 5a** and with a laminar water flow rate of 2.5 m/s. There are no recast layer or HAZ around the hole. In addition, the taper of the AFCH is close to zero when using LDIA + CWALD.

3.2 XRD analyses

Figure 6 shows XRD patterns of the substrate of the turbine blade and cross-sections of AFCHs. The as-received turbine blades mainly consist of γ-Ni ($Fm\bar{3}m$, a = 0.352 nm) and γ'-Ni_3Al ($Pm\bar{3}m$, ordered $L1_2$ structure, a = 0.357 nm). The intensity of the γ/γ' peaks is weakened obviously after the laser drilling. Besides the γ and γ' phases, α-Al_2O_3 ($R\bar{3}c$, a = 0.476 nm, c = 1.299 nm) and β-NiAl ($Pm\bar{3}m$, *B2* structure, a = 0.287 nm) formed in the cross-sections of the AFCHs drilled by LDIA. Compared with these AFCHs, only β-NiAl was added to the ones drilled by LDIA + CWALD.

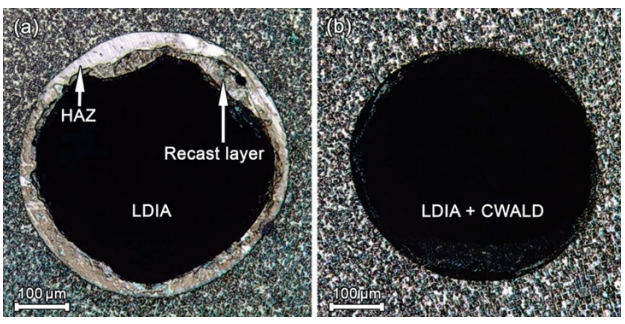

Figure 4: Microstructures of the cross-sections perpendicular to the drilling direction of the holes in an uncoated nickel-based single-crystal superalloy turbine blade operating at an average fluence of 65.03 J/cm^2 and v_w = 2.5 m/s: a) LDIA, b) LDIA + CWALD

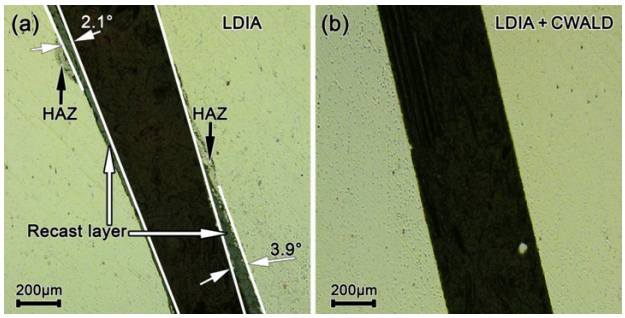

Figure 5: Microstructures of the cross-sections paralleled to the drilling direction of the AFCHs in an uncoated nickel-based single-crystal superalloy turbine blade operating at an average fluence of 65.03 J/cm^2 and v_w = 2.5 m/s: a) LDIA, b) LDIA + CWALD

3.3 SEM characterization

Figure 7a reveals the cross-sectional microstructure of the mid-section of an AFCH parallel to the direction of LDIA. It can be seen from **Figure 7a** that the local thickness of the oxide layer, recast layer and HAZ around the hole is up to 30 μm. Cracks formed between the recast layer and the substrate. **Figure 7b** reveals the cross-sectional microstructure of the mid-section of an AFCH parallel to the direction of LDIA + CWALD under the same parameters as in **Figure 7a**, with a laminar water flow rate of 2.5 m/s. This clearly indicates that no significant laser-induced damage such as oxide layer, recast layer or cracks occurred during CWALD.

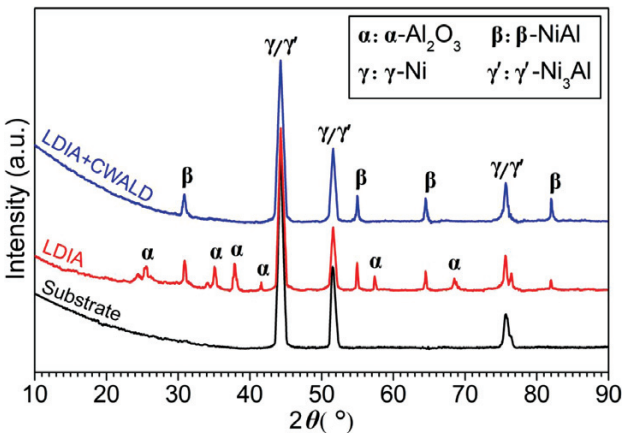

Figure 6: XRD patterns of the substrate of a turbine blade and cross-sections of the AFCHs drilled by LDIA and LDIA + CWALD

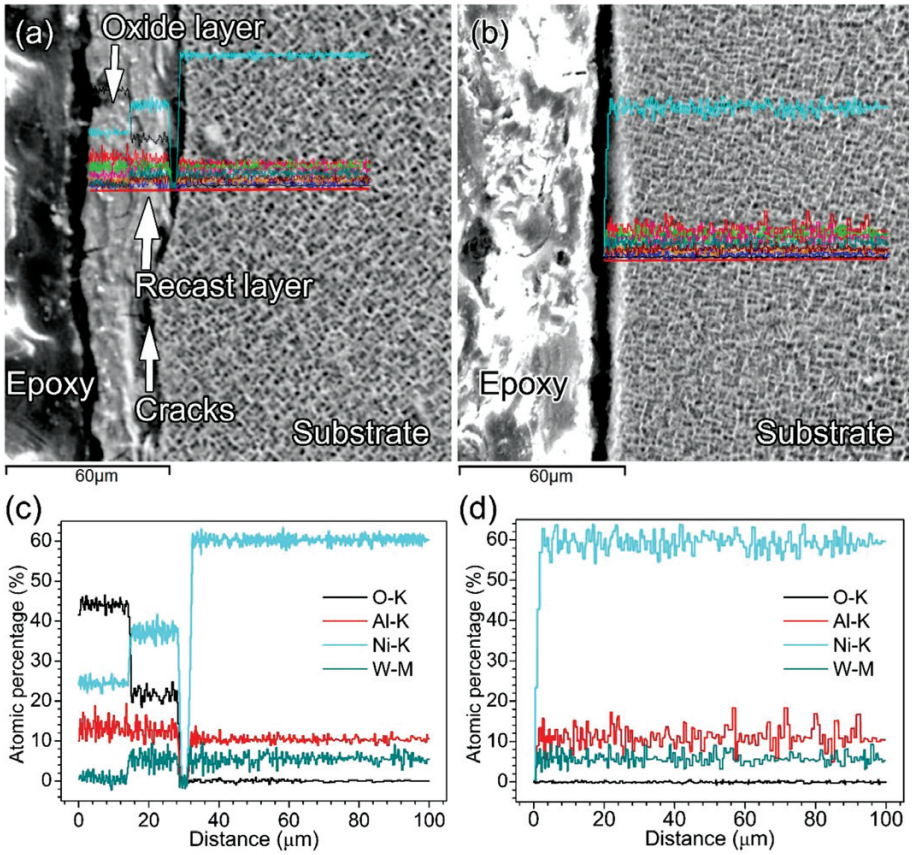

Figure 7: Microstructures and EDS of hole walls subjected to an average fluence of 65.03 J/cm^2 and v_w = 2.5 m/s: a) secondary electron scanning image of the AFCH drilled by LDIA, b) secondary electron scanning image of the AFCH drilled by LDIA + CWALD, c) line-scanning EDS of the red line marked in (a), d) line-scanning EDS of the red line marked in (b)

Figure 7c reveals the line-scanning EDS of the red line marked in **Figure 7a**. It can be seen from the figure that the atomic percentage of oxygen in the oxide layer is roughly 45 %. In the recast layer, the atomic percentage of oxygen is reduced to 20 %. The atomic percentage of nickel increases from the oxide layer to the substrate in a stepped transition. The atomic percentage of aluminum in the oxide layer and the recast layer is approximately 13 % and 10 %, respectively. The average atomic percentage of tungsten in the oxide layer is almost zero and it hardly changes in the recast layer and substrate. **Figure 7d** reveals the line-scanning EDS of the red line marked in **Figure 7b**. The atomic percentages of nickel, aluminum and tungsten are around 60 %, 11 % and 6 %, respectively, which are the same as those of the original materials in the substrate. The atomic percentage of oxygen is zero from the surface to the interior of the substrate. The atomic percentages of the rest of the elements contained in the original substrate did not change.

3.4 TEM investigation

Figure 8 exhibits the microstructures of the hole wall drilled by LDIA at a fluence of 65.03 J/cm^2 with minimum processing-induced defects. **Figure 8a** reveals the processing-induced defects, including a roughly 0.6 μm oxide layer, a roughly 1.5 μm recast layer, and a roughly 1.1 μm HAZ. **Figures 8b** and **8d** show the corresponding selected-area electron diffraction (SAED) patterns of primary phases in the oxide layer, recast layer and HAZ. Based on the SAED analysis, the oxide layer, recast layer and HAZ are mainly composed of α-Al_2O_3 (**Figure 8b**), γ-Ni (**Figure 8c**) and β-NiAl (**Figure 8d**), respectively. These results are completely consistent with those of XRD (**Figure 6**). SAED patterns for the regions marked with A, B and C in **Figure 8a** can be identified as the $[4\bar{2}\bar{2}3]$ zone axis of α-Al_2O_3, $[10\bar{1}]$ zone axis of γ-Ni, and [001] zone axis of β-NiAl, respectively.

Figure 9 exposes the microstructural and chemical features corresponding to the maximum and minimum processing-induced defects formed during LDIA + CWALD at a fluence of 65.03 J/cm^2 and a water flow rate of 2.5 m/s. **Figures 9a** and **9b** reveal that only the HAZ is induced by LDIA + CWALD in both locations with the maximum and minimum processing-induced defects. The HAZ thicknesses at the locations with the maximum and minimum processing-induced defects are up to approximately 2000 nm and 500 nm, respectively. **Figure 9c** shows the EDS for point "1" from **Figure 9b,** indicating that the HAZ contains mainly the chemical elements of nickel, aluminum and chromium. The atomic percentages of nickel, aluminum and chromium are

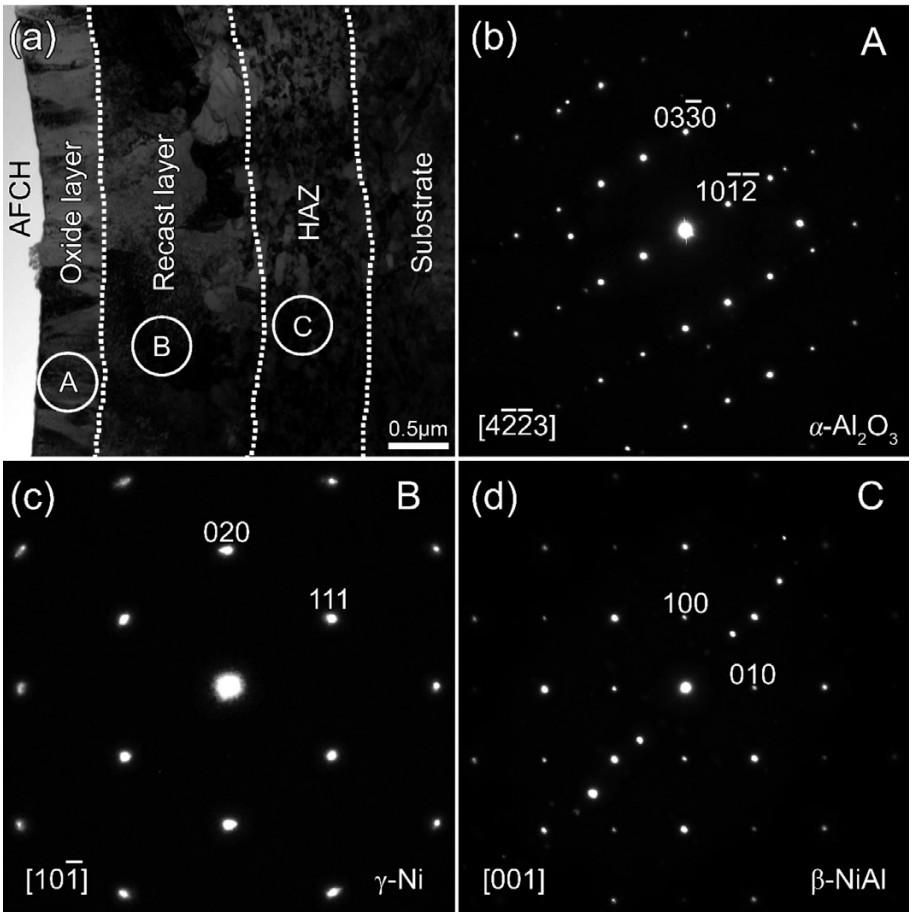

Figure 8: TEM images of the microstructures of the minimum processing-induced defects created during LDIA at an average fluence of 65.03 J/cm^2: a) bright field (BF) image of the hole wall, b) SAED pattern of the oxide layer, c) SAED pattern of the recast layer, d) SAED pattern of the HAZ

(52.08, 46.58 and 1.35) %, respectively. **Figure 9d** shows the SAED for the area marked with a white circle in **Figure 9b,** indicating that the HAZ is mainly composed of β-NiAl. The above results are fully consistent with those of XRD (**Figure 6**).

4 DISCUSSION

4.1 Microstructural evolution of the hole walls during LDIA and CWALD

The microstructural evolution of the sidewalls of the AFCHs may be attributed to element diffusion, oxidation and decomposition induced by the heat conduction during LDIA and CWALD. The oxyphilic aluminum in nickel-based superalloys is easily oxidized when the materials are exposed to a high temperature atmosphere.[18] α-Al_2O_3 is usually generated after the exposure to a temperature above 1000 °C in accordance with the following reaction:[19]

$$2\gamma\text{'-}Ni_3Al + 9[O] \rightarrow 6NiO + \alpha\text{-}Al_2O_3 \quad (1)$$

Due to the fact that the temperature of the focal point of the laser beam is higher than that of the vaporization point (4150 °C) of the nickel-based superalloys during LDIA, the heat accumulated around the AFCHs is at least higher than 1000 °C. In addition, the atmospheric air around the AFCHs contains oxygen, therefore the sidewalls of the AFCHs are covered with an oxide layer, mainly composed of α-Al_2O_3 as shown in **Figures 7a** and **9a**.

The γ-Ni phase (**Figure 8a**) in the recast layer of the AFCHs drilled by LDIA may result from the re-solidification of the basic constituent phase of the substrate, and/or from the decomposition of the γ'-Ni_3Al phase in the substrate. β-NiAl phases in the HAZ of AFCHs drilled by both LDIA and LDIA + CWALD result from the decomposition of γ'-Ni_3Al in the substrate. For the formation of β-NiAl, the literature reports that γ'-Ni_3Al in nickel-based superalloys can be decomposed into the γ-Ni phase and solid solution [Al] after experiencing heat conduction above 1000 °C.[20] When the solid solution [Al] diffuses to the surface of the substrate during LDIA and/or CWALD, the accumulation of [Al] in the HAZ increases as the heat conduction lasts and β-NiAl may be formed in accordance with the following reaction:[21]

$$\gamma\text{'-}Ni_3Al + 2[Al] \rightarrow 3\beta\text{-}NiAl \quad (2)$$

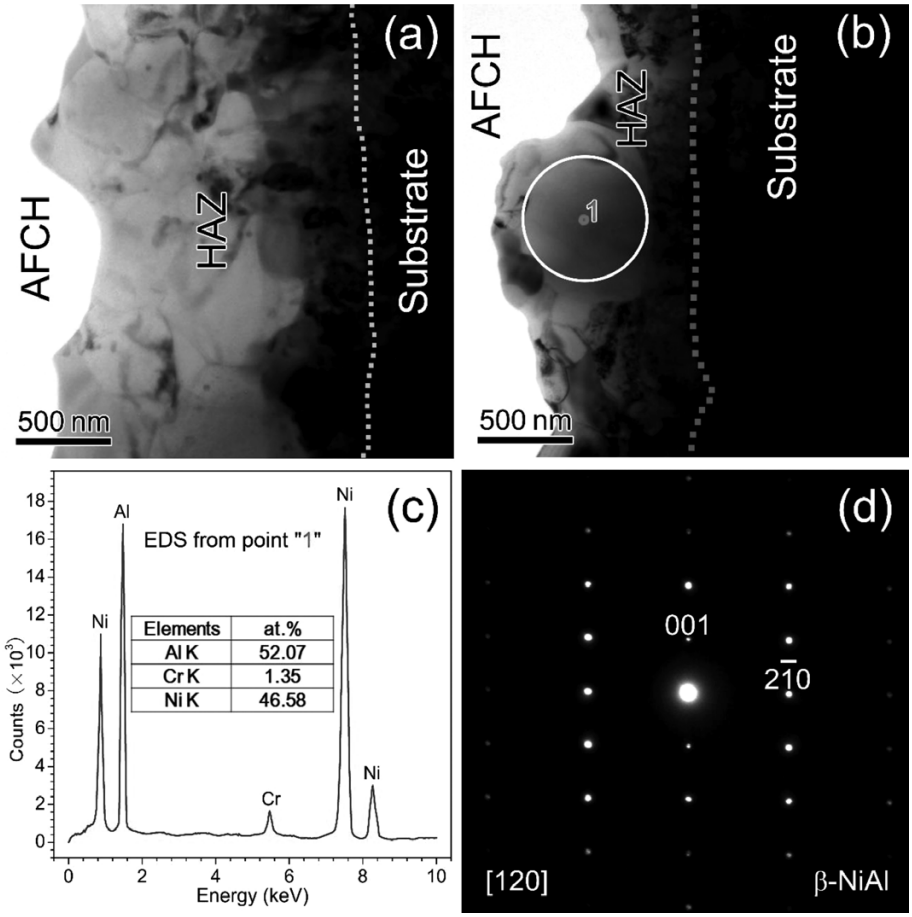

Figure 9: Microstructural and chemical features corresponding to the maximum and minimum processing-induced defects during LDIA + CWALD at a laser fluence of 65.03 J/cm^2 and water flow rate of 2.5 m/s: a) BF of the hole wall with the maximum processing-induced defects, b) BF of the hole wall with the minimum processing-induced defects, c) EDS for point "1" marked in (b), d) SAED for the region marked with a white circle in (b) that can be identified as the [120] zone axis of β-NiAl

4.2 Effect of coaxial waterjet on the processing-induced defects

During LDIA, the polarization of the laser beam changes due to multiple reflections, resulting in an irregular profile at the sidewalls of the AFCHs. However, the polarization of the laser beam is hardly changed in the case of laminar fluid water[22], thus the symmetry of the AFCHs drilled by LDIA + CWALD is higher than in the case of LDIA (**Figures 5** and **6**).

Typical recast layer and HAZ with thickness ranging from 10 μm to 1 mm are usually observed to be adjacent to the processing zones in nickel-based superalloys machined with conventional nanosecond lasers.[23] In this study, microstructural investigations of the material subjected to LDIA revealed that the thickness of the recast layer and HAZ was up to 100 μm (**Figures 7a** and **8a**). Fortunately, the AFCHs drilled by LDIA + CWALD at a laser fluence of 65.03 J/cm^2 and waterjet flow rate of 2.5 m/s clearly demonstrate the absence of common conventional processing-induced defects including spatters, oxide layer and recast layer (**Figures 3b, 5b, 6b, 7b, 9a** and **9b**). The absence of these defects mainly resulted from the effect of coaxial waterjet.

The material removal by means of laser machining depends on the laser power density, material properties and the time of the laser-matter interaction. The material removal by means of laser drilling generally includes the following three steps:[23] first, the target material absorbs the laser energy; second, the absorbed energy is redistributed within the target material; third, the target material is ablated by evaporation and/or melt ejection. The laser used in this study operates in the nanosecond regime (10^{-9} s) and its pulse duration is longer than the time for the energy transfer from electrons to the solid lattice, which usually takes several picoseconds (10^{-12} s). Therefore, the target material at the laser focal spot is heated by the absorbed laser energy. This energy is subsequently transferred to the surrounding by heat conduction. This procedure results in heat accumulation, consequently causing the melting and re-solidification of the ablated material, i.e., the recast layer and HAZ on the sidewalls of the AFCHs drilled by LDIA (**Figures 5** to **8**). Thermal stresses often result from the rapid heating and cooling of the target material during LDIA. The

cracks located at the interface between the recast layer and the substrate of the turbine blade are partially attributed to the tensile stresses, which developed during cooling due to a local contraction. Furthermore, thermal cycles between the laser pulses during LDIA also induce thermal stresses, aggravating the cracks. The results of this work suggest that interfacial cracks (**Figure 7**) may be induced by thermally induced stresses.

Since the processing-induced defects generated during LDIA are removed by the hole-expansion process of CWALD, the sidewalls of the AFCHs drilled by LDIA + CWALD are free of recast layer (**Figures 5** to **7** and **9**). The reduced defects of the AFCHs drilled by LDIA + CWALD are mainly due to the effect of coaxial waterjet. Water absorbs much more heat energy transformed from laser energy than superalloys after the increased temperature because the specific heat capacity of water is higher than that of solid materials. Heat energy from evaporated materials is principally absorbed by water through conduction and then washed away due to the high thermal conductivity. The volume percentage of oxygen in air is approximately 21 %, while in pure water it is about 3 %. Therefore, oxidation hardly takes place during CWALD, and the AFCHs are free of oxides. The ablated materials including spattered material, vaporized material, molten material and plasma debris are immediately washed away by coaxial waterjet so that the AFCHs are free of recast layer. Moreover, the cooling effect of coaxial waterjet restrains the heat accumulation around the AFCHs so that the thickness of the HAZ induced by LDIA + CWALD (**Figure 9**) is significantly smaller than that induced by LDIA (**Figure 8**).

4.3 Process and mechanism of LDIA + CWALD

In fact, the LDIA + CWALD process expands the holes drilled by LDIA. The apertures of AFCHs are smaller than the diameter of the coaxial waterjet. Accordingly, the flow rate of the water passing through the holes is higher than that of the coaxial waterjet, which strengthens the corresponding scouring effect of the water. Hence, the material removal rate of LDIA + CWALD is higher than that of LDIA. The mechanism of LDIA + CWALD is similar to that of CWALD, except that the processing efficiency of the former is higher than that of the latter.[24] This is due to the continuous flow of the water passing through the holes, which can limit the dynamic refraction of the laser beam and the ablated debris deposition.

Similar to CWALD, LDIA + CWALD follows a quasi-cold ablation process. When the coaxial waterjet contacts the surface of the workpiece, the height of the overflow water layer (h_f) can be calculated with Equation (3):[25]

$$h_f = \left(\frac{1+\eta\mu_i}{\sqrt[3]{g\nu_w}} \right) \sqrt{\frac{2\phi(1-\cos\theta)}{g\rho}} \tag{3}$$

Where η is the light absorption coefficient, μ_i is the inlet water flow rate, g is the gravitational acceleration, ν_w is the kinematic viscosity of waterjet, ϕ is the surface tension of water, θ is the contact angle of the material with water, and ρ is the water density.

Based on the conservation of mass, the velocity of the water passing through AFCHs (v_h) can be solved with Equation (4):

$$v_h = \frac{r_w \left[r_w v_w - 2h_f v_f \right]}{r_h^2} \tag{4}$$

where r_w is the radius of the waterjet, v_f is the velocity of the overflow water layer, and r_h is the radius of the AFCHs.

When the laser is transmitted through the water, the instantaneous distribution of energy density can be deduced from Equation (5):[24]

$$\psi(t) = \begin{cases} \xi \exp(-\beta t) - \exp(-\gamma t), & 0 \le t \le \tau \\ 0, & t > \tau \end{cases} \tag{5}$$

where ξ, β and γ are laser pulse shape parameters, and τ is the laser pulse duration.

Given the influence of the plasma plume, the final energy density of the laser on the focus spot can be expressed with Equation (6):[26]

$$I(z,t) = I_0(z,t) \exp\left[-((a v_h + c) z_p + b E_a(t)) \right] \tag{6}$$

where $I(z, t)$ is the final energy density of the laser on the focus spot, a, b and c are empirical coefficients, z_p is the ablation depth, and E_a is the laser energy density absorbed by the ablation plume.

The volumetric heat generated by laser drilling in water can be approximately calculated with Equation (7):[26]

$$A(x,y,z,t) = \alpha_m \exp(-\alpha_m z)(1-R_m) \exp(-\alpha_m h_f) \cdot \cdot (1-R_m) \exp\left[-((a v_h + c) z_p + b E_a(t)) \right] \frac{2P_0}{\pi\omega_0^2} \cdot \cdot \exp\left\{ \frac{-2\left[(x - v_x t)^2 + y^2 \right]}{\omega_0^2} \right\} \cdot \psi(t) \tag{7}$$

where α_m is the absorption coefficient of the workpiece material, α_w is the absorption coefficient of water, R_m is the reflectivity of the workpiece, R_w is the reflectivity of water, P_0 is the laser peak power, ω_0 is the radius of the laser beam at the focal position, and v_x is the laser traverse speed.

The above equations involve many parameters, and it is difficult to obtain exact solutions for all of them. However, the workpiece materials are ablated by volumetric heat. Furthermore, it can be seen from Equation (7) that the removal rate of the workpiece material is positively correlated with the flow rate of the coaxial waterjet.

Due to the laser scanning processing method, the workpiece materials are gradually ablated layer by layer, which induces overlap gaps between adjacent layers. These gaps cause tiny unevenness on the wall surfaces of

the AFCHs. Moreover, a high-pressure and high-temperature plasma plume is inevitably generated at the laser focal position because the laser fluence was set higher than the ablation threshold of the workpiece material. The plasma plume generates surface plasmon polaritons on the hole walls. With the interference between the incident laser and surface plasmons, the scanning paths of the laser beam at different layers are inconsistent and even changed greatly under the cooling effect of water. Therefore, the surface of a hole wall is uneven, as shown in **Figures 9a** and **9b**. Fortunately, the interference between the plasma plume, bubble explosion, surface plasmon polarization and second harmonic wave plays a certain positive role. The interference can partially convert the energy loss of the laser into impact power, increasing the strength and hardness of the thin layer around the AFCHs.

4.4 Potential influence of CWALD on AFCHs and turbine blades

During LDIA, the laser usually causes thermal damage including oxidation, recast layer and HAZ, which may induce stress concentration. Due to the presence of A1 and Ti in the nickel-based single-crystal superalloy substrate, turbine blades exhibit susceptibility to thermal cracking. Due to thermal stress, the thermal damage layers around the AFCHs are prone to crack along the circumferential and radial directions (**Figure 4**). Radial cracks in the thermal damage layers may expand to the substrate, reducing the fatigue life of the turbine blades. This is a potential hazard caused by LDIA. LDIA + CWALD significantly improve the processing quality of AFCHs and minimize the thermal damage (**Figures 4** to **9**); therefore, the above potential hazard is greatly reduced. Without the recast layer, AFCHs are free of taper, and the AFCH diameter is larger than in the case of LDIA. Furthermore, the roughness of the sidewall is also reduced. Under the same pressure of cooling air, the flow coefficient of AFCHs increases as the taper and the roughness of AFCHs decrease. The decrease in the taper and increase in the diameter not only reduce the vortex of cooling air, but also change the direction of the vortex. As a result, the flow direction of downstream cooling air at the center of the outlet is directed to the blade surface, effectively improving the adhesion of the cooling air to the blades. Thereby, all the above conditions can significantly improve the cooling efficiency of AFCHs and effectively protect turbine blades from erosion by high-temperature and high-speed gas. From these potential benefits, it can be inferred that LDIA + CWALD will become one of the main processing methods of drilling AFCHs in turbine blades. Furthermore, LDIA + CWALD will become more and more popular in the field of micro holing with high position precision in the future.

5 CONCLUSIONS

AFCHs drilled with LDIA and LDIA + CWALD were investigated in detail. Results clearly indicated that the maximum and minimum thicknesses of the processing-induced defects, such as oxide layer, recast layer, HAZ and cracks, around the sidewalls of the AFCHs drilled with LDIA are up to 100 μm and 3 μm, respectively. The main phases in the oxide layer, recast layer and HAZ are α-Al_2O_3, γ-Ni and β-NiAl, respectively. Except for the HAZ with a thickness ranging from 500–2000 nm, the AFCHs drilled with LDIA + CWALD are free from oxide layer, recast layer and cracks. As for the HAZ around the AFCHs drilled by LDIA + CWALD, the main phase is β-NiAl. The present work has proved that the asynchronous operation of LDIA + CWALD is a promising drilling technique for AFCHs of turbine blades with minimal processing-induced defects. The asynchronous operation of LDIA + CWALD may have wide application in micro holing and green manufacturing in the future.

Acknowledgment

This work was supported by the Natural Science Foundation of Zhejiang Province (Grant No. LY18E050027) and the Natural Science Foundation of Ningbo Municipality (Grant No. 2018A610145).

6 REFERENCES

[1] N. P. Padture, M. Gell, E. H. Jordan, Thermal barrier coatings for gas-turbine engine applications, Science, 296 (**2002**), 280–284, doi:10.1126/science.1068609

[2] Y. Dong, X. Li, Q. Zhao, X. Li, Y. Dou, Geometrical modeling to improve the accuracy of drilled cooling holes on turbine blades, Int. J. Adv. Manuf. Technol., 93 (**2017**), 4409–4428, doi:10.1007/s00170-017-0818-8

[3] J. Han, B. Yoo, H. J. Im, C. S. Oh, P. P. Choi, Microstructural evolution of the heat affected zone of a Co–Ti–W alloy upon laser cladding with a CoNiCrAlY coating, Mater. Charact., 158 (**2019**), 109998, doi:10.1016/j.matchar.2019.109998

[4] G. D. Gautam, A. K. Pandey, Pulsed Nd:YAG laser beam drilling: A review, Opt. Laser Technol., 100 (**2018**), 183–215, doi:10.1016/j.optlastec.2017.09.054

[5] M. Musztyfaga-Staszuk, D. Janicki, P. Panek, M. Wisniowski, Use of a laser disc for cutting silicon wafers, Mater. Tehnol., 52 (**2018**) 2, 139–142, doi:10.17222/mit.2017.052

[6] Y. F. Zhang, G. Y. Han, S. S. He, W. W. Yang, Microstructure evolution of in situ composite coatings fabricated by laser cladding with different powers, Mater. Tehnol., 55 (**2021**) 3, 419–425, doi:10.17222/mit.2020.194

[7] Y. H. Zhou, C. Li, Q. J. Zhou, S. W. Zhang, F. Xie, Effect of pulse duration on the properties of laser-welded glass joints, Mater. Tehnol., 56 (**2022**) 1, 27–32, doi:10.17222/mit.2021.217

[8] H. Mustafaa, D. T. A. Matthews, G. R. B. E. Römer, Investigation of the ultrashort pulsed laser processing of zinc at 515 nm: Morphology, crystallography and ablation threshold, Mater. Des., 169 (**2019**), 107675, doi:10.1016/j.matdes.2019.107675

[9] S. Pattanayak, S. Panda, Laser beam micro drilling – a review, Lasers Manuf. Mater. Process, 5 (**2018**), 366–394, doi:10.1007/s40516-018-0072-4

[10] C. M. Lee, W. S. Woo, J. T. Baek, E. J. Kim, Laser and arc manufacturing processes: a review, Int. J. Precis. Eng. Man., 17 (**2016**), 973–985, doi:10.1007/s12541-016-0119-4

[11] K. Hock, B. Adelmann, R. Hellmann, Comparative study of remote fiber laser and water-jet guided laser cutting of thin metal sheets, Phys. Procedia, 39 (**2012**), 225–231, doi:10.1016/j.phpro.2012.10.033

[12] B. Richerzhagen, Method and apparatus for machining material with a liquid-guided laser beam, PCT ed., Patent US5902499, US, 1999

[13] W. Zhang, Photon energy material processing using liquid core waveguide and a computer program for controlling the same, Patent US20060133752A1, US, 2006

[14] Y. K. Madhukar, S. Mullick, A. K. Nath, A study on co-axial water-jet assisted fiber laser grooving of silicon, J. Mater. Process Technol., 227 (**2016**), 200–215, doi:10.1016/j.jmatprotec.2015.08.013

[15] Y. Z. Liu, Coaxial waterjet-assisted laser drilling of air-film cooling holes in turbine blades, Int. J. Mach. Tool. Manu., 150 (**2020**), 103510, doi:10.1016/j.ijmachtools.2019.103510

[16] G. M. Hale, M. R. Querry, Optical constants of water in the 200-nm to 200-mm wavelength region, Appl. Optics, 12 (**1973**), 555–563, doi:10.1364/AO.12.000555

[17] J. F. Wei, L. Q. Sun, K. Zhang, X. Y. Hu, S. Zhou, Heat exchange model in absorption chamber of water-direct-absorption-typed laser energy meter, Opt. Laser Technol., 67 (**2015**), 65–71, doi:10.1016/j.optlastec.2014.09.015

[18] S. Pal, V. Kokol, N. Gubeljak, M. Hadzistevic, R. Hudak, I. Drstvensek, Dimensional errors in selective laser melting products related to different orientations and processing parameters, Mater. Tehnol., 53 (**2019**) 43, 551–558, doi:10.17222/mit.2018.156

[19] Y. Z. Liu, S. J. Zheng, Y. L. Zhu, H. Wei, X. L. Ma, Microstructural evolution at interfaces of thermal barrier coatings during isothermal oxidation, J. Eur. Ceram. Soc., 36 (**2016**), 1765–1774, doi:10.1016/j.jeurceramsoc.2016.02.011

[20] W. Li, Y. Li, C. Sun, Z. Hu, T. Liang, W. Lai, Microstructural characteristics and degradation mechanism of the NiCrAlY/CrN/DSM11 system during thermal exposure at 1100 °C, J. Alloy. Compd., 506 (**2010**), 77–84, doi:10.1016/j.jallcom.2010.06.168

[21] Y. Z. Liu, X. B. Hu, S. J. Zheng, Y. L. Zhu, H. Wei, X. L. Ma, Microstructural evolution of the interface between NiCrAlY coating and superalloy during isothermal oxidation, Mater. Des., 80 (**2015**), 63–69, doi:10.1016/j.matdes.2015.05.014

[22] A. Kruusing, Underwater and water-assisted laser processing: Part 2 – Etching, cutting and rarely used methods, Opt. Laser Eng., 41 (**2004**), 329–352, doi:10.1016/S0143-8166(02)00143-4

[23] Q. Feng, Y. N. Picard, H. Liu, S. M. Yalisove, G. Mourou, T. M. Pollock, Femtosecond laser micromachining of a single-crystal superalloy, Scripta Mater., 53 (**2005**), 511–516, doi:10.1016/j.scriptamat.2005.05.006

[24] V. Tangwarodomnukun, J, Wang, C. Z. Huang, H. T. Zhu, Heating and material removal process in hybrid laser-waterjet ablation of silicon substrates, Int. J. Mach. Tools Manu., 79 (**2014**), 1–16, doi:10.1016/j.ijmachtools.2013.12.003

[25] S. Duangwas, V. Tangwarodomnukun, C. Dumkum, Development of an overflow-assisted underwater laser ablation, Mater. Manuf. Process, 29 (**2014**), 1226–1231, doi:10.1080/10426914.2014.930896

[26] V. Tangwarodomnukun, Overflow-assisted laser machining of titanium alloy: surface characteristics and temperature field modeling, Int. J. Adv. Manuf. Technol., 88 (**2017**), 147–158, doi:10.4028/www.scientific.net/MSF.763.91